JGR Solid Earth

RESEARCH ARTICLE
10.1029/2019JB019271

Key Points:
- We present a new strategy for modifying kinetic models to consider the occurrence of channelization processes of pyroclastic material
- Two widely used kinetic models are modified by implementing this strategy: the energy cone and the box model
- We improve the accuracy of kinetic models without adding new, unconstrained input parameters

Supporting Information:
- Supporting Information S1

Correspondence to:
A. Aravena,
alvaro.aravenaponce@unifi.it

Citation:
Aravena, A., Cioni, R., Bevilacqua, A., de' Michieli Vitturi, M., Esposti Ongaro, T., & Neri, A. (2020). Tree-branching-based enhancement of kinetic energy models for reproducing channelization processes of pyroclastic density currents. *Journal of Geophysical Research: Solid Earth*, *125*, e2019JB019271. https://doi.org/10.1029/2019JB019271

Received 22 DEC 2019
Accepted 16 JUN 2020
Accepted article online 18 JUN 2020

©2020. American Geophysical Union. All Rights Reserved.

Tree-Branching-Based Enhancement of Kinetic Energy Models for Reproducing Channelization Processes of Pyroclastic Density Currents

A. Aravena[1], R. Cioni[1], A. Bevilacqua[2], M. de' Michieli Vitturi[2], T. Esposti Ongaro[2], and A. Neri[2]

[1]Dipartimento di Scienze della Terra, Università di Firenze, Florence, Italy, [2]Istituto Nazionale di Geofisica e Vulcanologia, Sezione di Pisa, Pisa, Italy

Abstract Kinetic energy models, also called kinetic models, are simple tools able to provide a fast estimate of the inundation area of pyroclastic density currents (PDCs). They are based on the calculation of the PDC front kinetic energy as a function of the distance from a source point. On a three-dimensional topography, the PDC runout distance is estimated by comparing the flow kinetic energy with the potential energy associated with the topographic obstacles encountered by the PDC. Since kinetic models do not consider the occurrence of channelization processes, the modeled inundation areas can be significantly different from those observed in real deposits. To address this point, we present a new strategy that allows improving kinetic models by considering flow channelization processes, and consists in the inclusion of secondary source points in the expected channelization zones, adopting a tree branch-like structure. This strategy is based on the redistribution of a key physical variable, such as the flow energy or mass depending on the considered kinetic model, and requires the adoption of appropriate equations for setting the characteristics of the secondary sources. Two models were modified by applying this strategy: the energy cone and the box model. We tested these branching models by comparing their results with those derived from their traditional formulations and from a two-dimensional depth-averaged model, considering two specific volcanoes (Chaitén and Citlaltépetl). Thereby, we show the capability of this strategy of improving the accuracy of kinetic models and considering flow channelization processes without including additional, unconstrained input parameters.

1. Introduction

Pyroclastic density currents (PDCs) are gravity-driven multiphase mixtures of hot particles (pyroclasts, lithics, and gas) generated by collapsing eruptive columns or volcanic domes (e.g., Druitt, 1998; Dufek et al., 2015; Shea et al., 2011; Sheridan et al., 2004; Sulpizio et al., 2014). They have velocities that can exceed 100 m/s (Belousov et al., 2007; Sheridan, 1979), highly variable volumes (from <0.01 km^3 to hundreds of cubic kilometers; Hayashi & Self, 1992), and maximum runout distances of up to 100 km in exceptionally large eruptions (Cas et al., 2011; Druitt, 1998; Roche et al., 2016). Consequently, PDCs represent one of the most hazardous processes associated with volcanic eruptions (e.g., Auker et al., 2013; Cole et al., 2015; García et al., 2011; Nakada, 2000; Neri, Esposti Ongaro, et al., 2015). For instance, the 2018 eruption of Fuego volcano (Guatemala) recently showed the catastrophic consequences that PDCs may produce, where a channelized flow traveled >10 km down slope and caused hundreds of fatalities. The main information source for studying the dynamics of PDCs derives from the analysis of pyroclastic deposits from past events (e.g., Branney & Kokelaar, 2002; Charbonnier & Gertisser, 2011; Dioguardi & Mele, 2018; Gurioli et al., 2010; Komorowski et al., 2013; Sandri et al., 2014; Shea et al., 2011; Sheridan, 1979; Sulpizio et al., 2014; Valentine et al., 2000). However, considering the topographic effect on the transport dynamics of PDCs and the continuous variation of topography in volcanic areas, the involvement of additional tools is required to properly study the hazard associated with PDCs. Several numerical models have been developed in order to assess this hazard, such as energy cone model (e.g., Malin & Sheridan, 1982; Ogburn & Calder, 2017), box model (e.g., Bonnecaze et al., 1995; Dade & Huppert, 1996; Esposti Ongaro et al., 2016; Huppert & Simpson, 1980), FLOW3D (e.g., Saucedo et al., 2005; Sheridan et al., 2004), Titan2D (e.g., Murcia et al., 2010), VolcFlow (e.g., Kelfoun, 2011; Kelfoun et al., 2009), PDAC (e.g., Esposti Ongaro et al., 2007; Esposti Ongaro et al., 2019; Neri et al., 2003), and IMEX_SfloW2D (de' Michieli Vitturi et al., 2019). Roche et al. (2013)

classified these models in four types: kinetic, discrete element, depth-averaged, and multiphase models. Even if Roche et al. (2013) did not consider the box model approach in their classification, we suggest that it can be included in the kinetic model class because it provides a physically based law for the kinematics of the flow front. In general, kinetic models are based on the calculation of the kinetic energy in the flow front as a function of the distance traveled by the PDC. Kinetic energy is compared with the potential energy associated with the topographic obstacles encountered by the PDC to calculate the runout distance. Because kinetic models are able to generate results rapidly, they have been adopted to assess volcanic hazard using a probabilistic approach (Aspinall et al., 2019; Bevilacqua et al., 2017; Neri, Esposti Ongaro, et al., 2015; Sandri et al., 2018; Tierz, Sandri, Costa, Sulpizio, et al., 2016; Tierz, Sandri, Costa, Zaccarelli, et al., 2016). This approach allows the consideration of the natural variability observed in the eruptive process by sampling the model input parameters within their expected variation ranges, as shown in Tierz, Sandri, Costa, Zaccarelli, et al. (2016), where the energy cone model was systematically applied to capture the variability of relevant parameters for hazard assessment (e.g., inundation area and maximum runout distance) in Somma-Vesuvius and Campi Flegrei (Italy). However, kinetic models significantly simplify the physics of the problem (Roche et al., 2013) and, in particular, are not able to properly describe flow channelization. Thus, the resulting inundation areas can be significantly different from those observed in nature and estimated with other numerical models, particularly in terms of runout distance along ravines (e.g., Ogburn & Calder, 2017; Tierz, Sandri, Costa, Zaccarelli, et al., 2016). Considering the influence of flow channelization in PDC propagation and runout distance, as evidenced during the 2018 Fuego eruption, its proper inclusion in numerical models is of paramount importance for volcanic hazard assessment.

In this context, we present a new strategy for modifying kinetic models to consider the channelization of pyroclastic material. We illustrate and implement this methodology by adopting two widely used kinetic models: the energy cone and the box model (Esposti Ongaro et al., 2016; Neri, Esposti Ongaro, et al., 2015; Sheridan et al., 2004; Sheridan & Malin, 1983; Tierz, Sandri, Costa, Zaccarelli, et al., 2016; Wadge & Isaacs, 1988). Both have been applied in a statistical framework, by sampling the variability range of model input parameters and by comparing the numerical results on the *ensemble* of simulations. This allows to capture the uncertainty in PDC generation/propagation conditions and is particularly useful because kinetic models are extremely sensitive to few empirical parameters, and calibration can a priori only define a range of values.

This work consists of five parts. First, we describe the strategy proposed here for modifying kinetic models by considering the occurrence of channelization processes. Second, we present the application of this strategy to the energy cone and box model. Third, we test these models by comparing their results with the traditional energy cone and box model, with real PDC deposits and with other numerical tools, considering two specific volcanoes as reference case studies (Chaitén, Chile, and Citlaltépetl, Mexico; the input and main output parameters of all the simulations described in this work are presented in Tables S1–S4 in the supporting information). Finally, we discuss the applicability of this modeling strategy and conclude with a summary of results and potential use of this approach in future hazard assessment studies.

2. The Proposed Strategy

Kinetic models are typically based on an integral dissipation law of a key physical variable (Φ). This variable is energy in the energy cone model, dissipated by granular friction, and inertia in the box model, dissipated by sedimentation. In both models, the source conditions are associated with the gravitational collapse of a gas-pyroclast mixture, so that the initial values of Φ are controlled by the initial potential energy and the initial mass, respectively. In any kinetic model, a function $H(r, \theta)$ is derived, which represents the maximum topographic height that can be overpassed by the PDC (Figure S1), where r is the distance from the source position (P) and θ is the polar angle of the propagation direction. $H(r, \theta)$ is a monotonically decreasing function and defines a conoid, whose center is located in the PDC source position (Figure S1). The intersection between this conoid and volcano topography delineates the function $d(\theta)$, representing the PDC runout distance in the propagation direction θ. In kinetic models, when topography blocks the flow, the residual part of the physical variable Φ is immediately dissipated. In the strategy presented here, we assume instead that the residual part of Φ is redistributed in the adjacent cells along topographic channels, with the kinetic model applied iteratively with new branching sources.

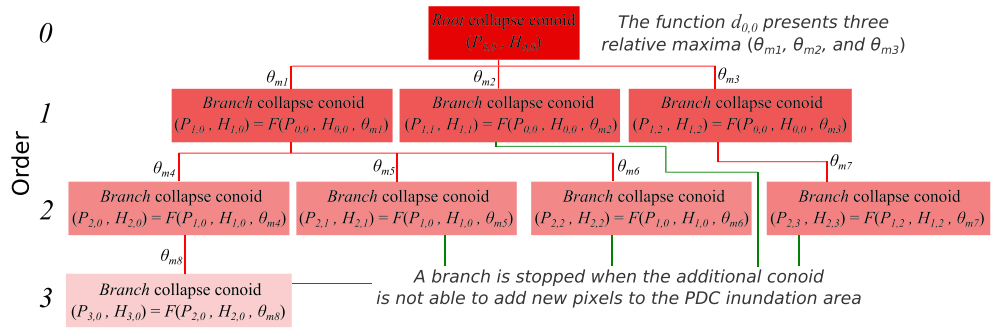

Figure 1. Structure of the branching strategy presented here for modifying kinetic models to include flow channelization processes.

To introduce the mathematical formalism, we define a *root* conoid (with order $i = 0$ and index $j = 0$), characterized by the source position $P_{0,0}$ and by the function $H_{0,0}(r, \theta)$, which is complemented with additional source conoids (*branch* conoids) located in the domains of preferential channelization of pyroclastic material (Figure 1). Each *branch* conoid (with order $i > 0$ and index j, which is a variable introduced to discriminate the different *branch* conoids of the same order) is characterized by the source position $P_{i,j}$ and by the function $H_{i,j}(r, \theta)$. $P_{i,j}$ and $H_{i,j}(r, \theta)$ are controlled exclusively by the properties of the parent conoid (i.e., with order $(i - 1)$ and index k) and by the volcano topography, whose interplay defines the function of horizontal distance $d_{i-1,k}(\theta)$ as described previously. This process is repeated in a tree branch structure that is stopped when the *branch* conoids are not capable of adding new pixels to the resulting inundation area (Figure 1). Thereby, the PDC inundation area is defined by the union of the inundation areas associated with each conoid.

This tree branch-like structure defines a particular branching process (Asmussen & Hering, 1983; Harris, 1963) in which the number and properties of the offspring conoids depend on the footprint of their parent conoids over topography (Haccou et al., 2005). The mathematical properties of the branching process $[P_{i,j}, H_{i,j}(r, \theta)]$ are not trivial, and the direct numerical simulation is the only feasible modeling approach. We will show that, under our modeling conditions (i.e., considering the energy dissipation law adopted in the energy cone model and the sedimentation equation adopted in the box model), the number of generations that significantly increase the inundation area is bounded. In other words, the inundated area converges to a finite value when the number of generations tends to infinity.

2.1. Energy Cone

The energy cone is the simplest model able to estimate the maximum runout and inundation area of PDCs. It was proposed by Malin and Sheridan (1982) to model the 1980 blast eruption of Mount St. Helens and has been repeatedly employed for assessing volcanic hazard at high risk volcanoes (Alberico et al., 2002; Sandri et al., 2018; Sheridan et al., 2004; Sheridan & Malin, 1983; Tierz, Sandri, Costa, Sulpizio, et al., 2016; Tierz, Sandri, Costa, Zaccarelli, et al., 2016; Wadge & Isaacs, 1988). The applicability field of this model should be limited to frictional granular flows (i.e., characterized by particle volume concentration higher than about 0.3), but it has been adopted to describe pyroclastic currents in a broader range of concentrations (Alberico et al., 2002; Sheridan & Malin, 1983). This model considers that the potential energy (in this case, the key physical variable Φ) of pyroclastic material reaching a height H_c above the vent is converted into kinetic energy as the material collapses and moves laterally away from the vent (Sheridan & Malin, 1983). A constant rate of energy dissipation defines a cone with vertical axis (from which the term *energy cone* is used instead of the more generic term *conoid*), whose slope φ is function of a friction parameter μ (Heim coefficient; Hsu, 1975; Malin & Sheridan, 1982; Sheridan et al., 2004) and whose apex is the collapse height H_c. The parameters φ and H_c have been typically calibrated using the maximum runout distance (L) of past PDCs (Hayashi & Self, 1992; Ogburn & Calder, 2017; Sheridan et al., 2004), so that H/L has become a common notation for $\tan(\varphi)$, where H is the vertical distance between the collapse height and the topographic height associated with the maximum runout position.

In this model, $H(r, \theta)$ is given by

$$H(r, \theta) = H(r) = H_c - r \cdot \tan(\varphi) \tag{1}$$

and thus goes to 0 (i.e., no residual part) when $r = H_c/\tan(\varphi)$.

2.1.1. Branching Formulation

If we adopt the strategy proposed in this work, Equation 1 is only valid for the *root* energy cone (i.e., $H_{0,0}(r, \theta) = H(r, \theta)$), while the general equation for the function $H_{i,j}(r, \theta)$ associated with a generic energy cone of order i, index j, and source position $P_{i,j} = (x_v, y_v)$ is given by

$$H_{i,j}(r, \theta) = H_{i,j}(r) = H_{c(i,j)} - r \cdot \tan(\varphi) \tag{2}$$

where $H_{c(i,j)}$ is the apex height of the generic energy cone of order i and index j. Here we assume a constant value of φ for all the generations of energy cones.

Let consider a given propagation direction, defined by the polar angle θ_o, where topography is characterized by a relatively high elevation (such as θ_{01} and θ_{02} in Figures 2c and 2e). Because the potential energy may not be large enough to overcome this high-elevation zone, this propagation direction is expected to present a relatively low value of $d_{i,j}(\theta)$, as observed in Figure 2e for θ_{01} and θ_{02} ($d_{i,j}(\theta)$ represents the function of horizontal distance associated with the energy cone of order i and index j, calculated at angle intervals of 10° in the simulations presented in this work). In contrast to the traditional energy cone formulation, here we redistribute the residual potential energy derived from propagation directions characterized by low values of $d_{i,j}(\theta)$ in the adjacent relative maxima of $d_{i,j}(\theta)$ (θ_{m1} and θ_{m2} in the example shown in Figures 2c and 2e). This is proposed because, considering that $H_{i,j}(r, \theta)$ is a decreasing function of r, the relative maxima of $d_{i,j}(\theta)$ represent the directions where topographic elevation tends to be low (e.g., ravines), and thus, flow channelization likely occurs in these directions. We assume that all the relative maxima of $d_{i,j}(\theta)$ represent points of preferential channelization, and thus, they are the origin of additional energy cones of order $(i+1)$. The source position of the $(i+1)$-order energy cone associated with the relative maximum θ_m, defined using the index k, is given by

$$P_{i+1,k} = P_{i+1,k}(\theta_m) = \left(x_v + d_{i,j}(\theta_m) \cdot \cos(\theta_m), y_v + d_{i,j}(\theta_m) \cdot \sin(\theta_m)\right) \tag{3}$$

The redistributed residual energy (E_r) of the relative minimum θ_o in the adjacent relative maximum θ_m satisfies

$$E_r(\theta_o, \theta_m) \propto \left(d_{i,j}(\theta_m) - d_{i,j}(\theta_o)\right) \cdot \tan(\varphi) \tag{4}$$

Please note that $(d_{i,j}(\theta_m) - d_{i,j}(\theta_o)) \cdot \tan(\varphi)$ represents the elevation difference between the runout points associated with the propagation directions θ_o and θ_m. Accordingly, the variable $H_{c(i+1,k)}$ needed to calculate $H_{i+1,k}(r, \theta)$ (Equation 2) for the additional energy cone of order $(i + 1)$ associated with the relative maximum θ_m is given by

$$H_{c(i+1,k)} = H_{c(i+1,k)}(\theta_m) = \frac{1}{2\pi}\int_{\theta_1}^{\theta_2}\left(d_{i,j}(\theta_m) - d_{i,j}(\theta)\right) \cdot \tan(\varphi) d\theta \tag{5}$$

where θ_1 and θ_2 represent the limits of the portion of the energy cone of order i and index j that is able to be channelized through the relative maximum θ_m. Specifically, the angles θ_1 and θ_2 are associated with the relative minima immediately adjacent to the relative maximum θ_m (in the example presented in Figure 2, the integration limits are θ_{01} and θ_{02}). In order to avoid the backward movement of pyroclastic material between a given energy cone of order i and its offspring, for $i > 0$, the propagation of material is only considered in directions whose angle with respect to the previous propagation direction is equal or lower than 90°. This assumption still allows modeling tight curves when they involve more than two generations of energy cones, as observed in Figure 3a (e.g., at east of the vent).

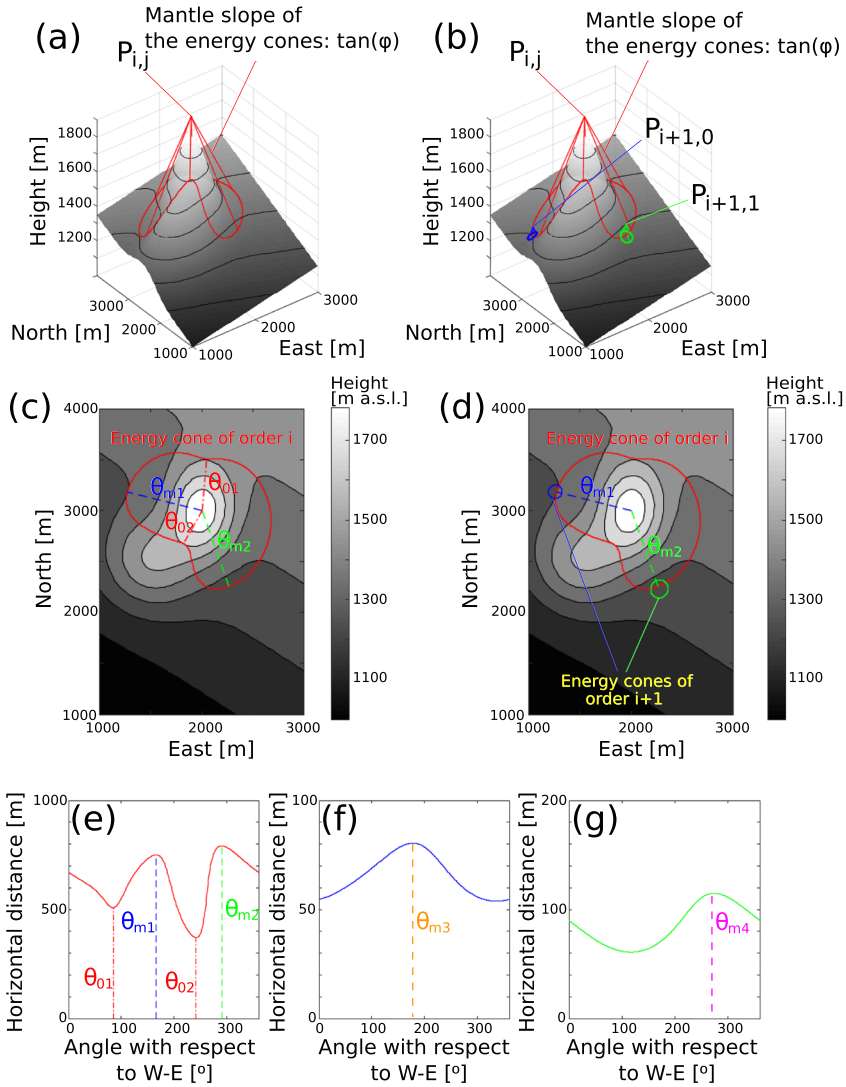

Figure 2. (a) Surface plot of a generic i-order energy cone and the topography. (b) Surface plot of a generic i-order energy cone, the derived $(i+1)$-order energy cones, and the topography. (c) Contour plot of a generic i-order energy cone and the topography. (d) Contour plot of a generic i-order energy cone, the derived $(i+1)$-order energy cones, and the topography. (e) Function of horizontal distance $d_{i,j}(\theta)$. (f and g) Functions of horizontal distance $d_{i+1,k}(\theta)$ associated with the relative maxima θ_{m1} and θ_{m2} of the function $d_{i,j}(\theta)$, respectively. The relative maxima (θ_{m3} and θ_{m4}) of these functions represent the origin of $(i+2)$-order energy cones.

Considering this formulation in an iterative scheme, it is possible to construct a tree branch-like structure of energy cones able to redistribute the flow residual potential energy into channels. Like the traditional energy cone model, the only input parameters of the branching formulation are $P_{0,0}$, H_c (equal to $H_{c(0,0)}$), and φ. Figure 3a presents the inundation area of an illustrative, single simulation where the blue points represent the apex position of all the energy cones computed by the code, and the inundation area associated exclusively with the *root* energy cone is indicated by a yellow line (Table S1). This simulation produces 15 orders of energy cones (61 energy cones), characterized by decreasing values of $H_{c(i,j)}$ (Figures 3b and 3c).

2.2. Box Model

The box model integral formulation for inertial, gravity-driven particle currents is based on the pioneering work of Huppert and Simpson (1980) and corresponds to a simplified system of ordinary differential

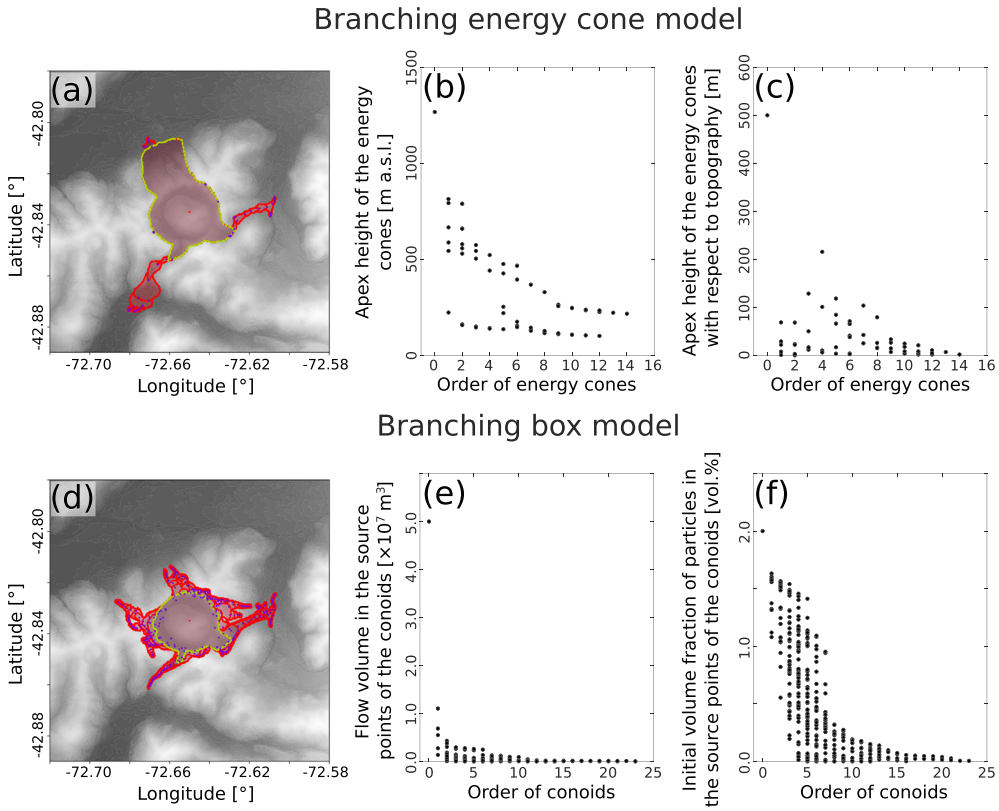

Figure 3. Results associated with illustrative simulations of the branching energy cone (a–c) and box model (d–f), considering the Chaitén volcano topography. (a) Inundation map. The blue points represent the position of all the energy cones computed in this model. The inundation area associated exclusively with the *root* energy cone is indicated by a yellow line. (b and c) Apex height of the energy cones (with respect to the sea level and topography, respectively) reported as a function of their order. (d) Inundation map. The blue points represent the source position of all the conoids computed in this model. The inundation area associated exclusively with the *root* conoid is indicated by a yellow line. (e) Collapsing volume ($V_{i,j}$) in the *root* and *branch* conoids reported as a function of their order. (f) Initial volume fraction of particles ($\phi_{0,(i,j)}$) in the *root* and *branch* conoids reported as a function of their order. Input parameters are described in Tables S1 and S4.

equations able to describe the propagation dynamics of PDCs in the inertial regime (the general theory is detailed in Bonnecaze et al. (1995) and Hallworth et al. (1998)). This model is applicable to regimes in which friction is negligible with respect to inertial terms, such as relatively dilute flows (particle concentration $<10^{-2}$). In any case, the applicability of the box model to a broader range of flow conditions in simplified geometries has been shown experimentally and numerically (Esposti Ongaro et al., 2016; Gladstone & Woods, 2000). In this model, a constant flow volume (gas and pyroclasts) is assumed, and thus, we consider particle volume fraction (ϕ), instead of mass, as the dissipated variable Φ of this model (Esposti Ongaro et al., 2016). During PDC propagation, the current loses inertia (i.e., mass) and the maximum runout can be calculated in terms of the sedimentation rate. In this work, all the solid particles are assumed to have the same size, shape, and density, and thus to deposit at the same velocity, which allows us to have an analytical solution (instead, polydisperse formulation can only be solved numerically). Ambient fluid entrainment is neglected and thermal properties of the flow are assumed to remain constant with no consideration of hot gas buoyancy with respect to the ambient gas. We also assume an axisymmetric geometry. This model allows estimating the temporal evolution of front velocity, average current depth, and depth-averaged particle concentration. Further description of this approach is provided in Biagioli et al. (2019) and Bevilacqua (2016, 2019).

The model is based on the Von Kármán equation for density currents:

$$\frac{dL(t)}{dt} = Fr\sqrt{h(t)g\frac{\rho_c(t)-\rho_a}{\rho_a}} \tag{6}$$

where $L(t)$ and $h(t)$ are the radial distance reached by the current and its height as a function of time (t), Fr is the Froude number (i.e., nondimensional number defined as the ratio of inertial and gravitational forces), g is gravity, ρ_a is ambient fluid density, and $\rho_c(t)$ is density of the current at time t:

$$\rho_c(t) = \phi(t)\rho_p + (1-\phi(t))\rho_a \tag{7}$$

where ρ_p is density of the solid particles and $\phi(t)$ is solid particle volume fraction at time t, described by

$$\frac{d\phi(t)}{dt} = -w_s\frac{\phi(t)}{h(t)} \tag{8}$$

where w_s is the sedimentation velocity of particles.

Since the volume V of the current (i.e., gas and pyroclasts) is preserved and its geometry is axysymmetric, we have

$$V = L(t)^2 h(t)\pi = const \tag{9}$$

In summary,

$$\begin{cases} \dfrac{dL(t)}{dt} = Fr\sqrt{h(t)\phi(t)g\dfrac{\rho_p-\rho_a}{\rho_a}} \\ \dfrac{d\phi(t)}{dt} = -w_s\dfrac{\phi(t)}{h(t)} \\ V = L(t)^2 h(t)\pi \end{cases} \tag{10}$$

As described in Text S1, from this system of differential equations, we can derive equations for the maximum runout distance reached by the flow in absence of topography (L_{max}, Equation 11) and the function $H(r,\theta)$ that computes the maximum obstacle height that the PDC is capable of overpassing (Equation 12).

$$L_{max} = \left[8\frac{Fr\cdot\phi_0^{1/2}\cdot g_p^{1/2}\cdot(V/\pi)^{3/2}}{w_s}\right]^{1/4} \tag{11}$$

$$H(r,\theta) = H(r) = \frac{1}{2g}\left(\frac{C\cdot L_{max}^{1/3}}{\left(\frac{r}{L_{max}}\right)\cosh^2\left(\operatorname{arctanh}\left(\left(\frac{r}{L_{max}}\right)^2\right)\right)}\right)^2 \tag{12}$$

where ϕ_0 is the initial volume fraction of particles in the PDC, and we use the short notations $g_p := g\frac{\rho_p-\rho_a}{\rho_a}$ and $C := (Fr^2 w_s\phi_0 g_p)^{1/3}/2$. The influence of different box model input parameters on numerical results is described in Esposti Ongaro et al. (2016).

2.2.1. Branching Formulation

A generic conoid of order i and index j is defined by its source position $P_{i,j} = (x_v, y_v)$ and by $H_{i,j}(r,\theta)$, obtained from Equation 12:

$$H_{i,j}(r,\theta) = h_{min,(i,j)}(r,\theta) + \frac{1}{2g}\left(\frac{C_{i,j}\cdot L_{max,(i,j)}^{1/3}}{\left(\frac{r}{L_{max,(i,j)}}\right)\cosh^2\left(\operatorname{arctanh}\left(\left(\frac{r}{L_{max,(i,j)}}\right)^2\right)\right)}\right)^2 \tag{13}$$

where $h_{min,(i,j)}(r,\theta)$ is the minimum topographic height reached by the flow in the segment between $P_{i,j}$ and $P_{i,j}+(r\cdot\cos(\theta), r\cdot\sin(\theta))$, $C_{i,j}$ is given by Equation 14, and $L_{max,(i,j)}$ is given by Equation 15.

$$C_{i,j} = \frac{\left(Fr^2 w_s \phi_{0,(i,j)} g_p\right)^{1/3}}{2} \tag{14}$$

$$L_{max,(i,j)} = \left[8\frac{Fr \cdot \phi_{0,(i,j)}^{1/2} \cdot g_p^{1/2} \cdot \left(V_{i,j}/\pi\right)^{3/2}}{w_s}\right]^{1/4} \tag{15}$$

where $\phi_{0,(i,j)}$ is the initial volume fraction of particles in the conoid of order i and index j, and $V_{i,j}$ is the associated collapsing volume. We remark that the collapsing volume of the whole PDC is given by $V_{0,0}$, while $V_{i,j}$ is a fraction of the initial volume ($V_{0,0}$) when $i > 0$.

During transport, particle concentration in the PDC is

$$\phi_{i,j}(r) = \left[\left(\phi_{0,(i,j)}\right)^{1/2} - \frac{1}{8}\left(\frac{w_s}{Fr}\right) g_p^{-1} \left(\frac{V_{i,j}}{\pi}\right)^{-3/2} r^4\right]^2 \tag{16}$$

Let consider a propagation direction defined by the polar angle θ_o and characterized by the presence of a topographic obstacle. Because the residual inertia may not be large enough to overcome this obstacle, this propagation direction is expected to present a relatively low value of $d_{i,j}(\theta)$. In contrast to the traditional box model, here we redistribute the residual (i.e., not sedimented) pyroclastic material derived from the propagation directions characterized by low values of $d_{i,j}(\theta)$ in the adjacent relative maxima of the function $d_{i,j}(\theta)$, which are defined using an angle step of 10°. For that, we assume that the initial particle concentration of the flow volume redistributed in the relative maximum θ_m, defined using the index k, satisfies

$$\phi_{0,(i+1,k)} = \phi_{0,(i+1,k)}(\theta_m) = \frac{1}{\theta_2 - \theta_1}\int_{\theta_1}^{\theta_2} \phi_{i,j}\left(d_{i,j}(\theta)\right) d\theta \tag{17}$$

where θ_1 and θ_2 represent the limits of the portion of the conoid of order i and index j that is able to be channelized through the relative maximum θ_m (specifically, θ_1 and θ_2 are the angles of the relative minima immediately adjacent to the relative maximum θ_m). All the relative maxima of $d_{i,j}(\theta)$ represent points of preferential channelization, and thus they are the origin of *branch* conoids of order $(i+1)$. Also in this case, in order to avoid the backward movement of pyroclastic material, for $i > 1$, the transport of material is only considered in propagation directions whose angle with respect to the previous transport direction is equal or lower than 90°. The central position of the additional source conoid of order $(i+1)$ associated with the relative maximum θ_m is given by

$$P_{i+1,k} = \left(x_v + d_{m,(i,j)}(\theta_m) \cdot \cos(\theta_m), y_v + d_{m,(i,j)}(\theta_m) \cdot \sin(\theta_m)\right) \tag{18}$$

where $d_{m,(i,j)}(\theta_m)$ is defined following Equation 19, while the redistributed flow volume is given by Equation 20.

$$d_{m,(i,j)}(\theta_m) = \frac{1}{\theta_2 - \theta_1}\int_{\theta_1}^{\theta_2} d_{i,j}(\theta) \cdot \cos(\theta - \theta_m) d\theta \tag{19}$$

$$V_{i+1,k}(\theta_m) = \frac{\theta_2 - \theta_1}{2\pi} \cdot V_{i,j} \cdot \frac{1 - \phi_{0,(i,j)}}{1 - \phi_{0,(i+1,k)}(\theta_m)} \tag{20}$$

This expression derives from the conservation of the PDC gas and the initial particle concentration of the $(i+1)$-order conoid associated with the relative maximum θ_m. Accordingly, considering the updated values of $V_{i+1,k}$ and $\phi_{0,(i+1,k)}$, it is possible to calculate the variables $C_{i+1,k}$ and $L_{max,(i+1,k)}$, and thus the function $H_{i+1,k}(r, \theta)$ needed to fully define the *branch* conoid.

Using an iterative scheme, we can construct a tree branch-like structure of conoids able to redistribute the flow residual mass into channels. The iterative formulation does not need additional input parameters, and, like the traditional box model, the input variables are source position ($P_{0,0}$), Froude number (Fr),

sedimentation velocity (w_s), initial volume fraction of particles ($\phi_{0,(0,0)}$), collapsing volume ($V_{0,0}$), particle density (ρ_p), and ambient fluid density (ρ_a). Figure 3d presents the inundation area of an illustrative, single simulation of this model, where the blue points represent the central positions of all the conoids computed by the program, while the inundation area associated exclusively with the *root* conoid is indicated by a yellow line (input parameters are presented in Table S4). This simulation presents 24 orders of conoids (383 conoids), characterized by decreasing values of $V_{i,j}$ and $\phi_{0,(i,j)}$ (Figures 3e and 3f). The calculation time of the branching box model tends to be significantly higher than the calculation time needed by the branching energy cone model.

3. Test Simulations

Here we present some simulations aimed at testing the ability of these models to consider channelization processes and reproduce the expected inundation area of PDCs, while the applicability of these models to different volcanological cases is discussed in section 4. In this section, Chaitén (Chile) and Citlaltépetl (Mexico) volcanoes were adopted as reference case studies. Both volcanoes present topographic features able to produce a strong control on the distribution of pyroclastic material during the transport of PDCs. The topographic information considered in numerical simulations derives from the SRTM 30 m elevation data (Rabus et al., 2003). We remark that kinetic models are not particularly affected by digital elevation model (DEM) resolution (e.g., Tierz, Sandri, Costa, Sulpizio, et al., 2016), and the adopted elevation data have shown to be enough precise for the simulations presented here. For Chaitén volcano, we consider the PDC deposits associated with the 2008–2009 eruption, which was characterized by an initial Plinian phase (column height of 18–20 km) with minor pyroclastic flows derived from column collapse, followed by various cycles of lava dome growth and collapse, producing directed, additional PDCs (Carn et al., 2009; Lara, 2009; Major et al., 2013; Major & Lara, 2013). For Citlaltépetl volcano, we consider the numerical results described by Sheridan et al. (2004), who studied the PDC deposits associated with some well-documented volcanic events by adopting two numerical models: the energy cone and FLOW3D.

3.1. Branching Energy Cone

Figures 4a–4d present a map of the zones covered by the PDC deposits derived from the 2008–2009 Chaitén eruption (Figure 4a), and the inundation areas associated with three sets of simulations developed by using the branching and traditional energy cone models (Figures 4b–4d and Table S1). In particular, Figure 4b presents the results of a set of simulations ($N = 300$, where N is the number of simulations) performed by adopting the branching formulation, where we use input parameters variable within specific ranges ($P_{0,0} = (-72.650°, -42.835°)$, considering a 500 mradius variability zone, $H_c = 200 - 1000$ m above topography, and $\tan(\varphi) = 0.35 - 0.45$, i.e., $\varphi \approx 19° - 24°$), which allow capturing a wide set of PDC formation/propagation conditions. The resulting map describes the fraction of simulations that reaches each pixel of the studied zone. In this case, when results are compared with the traditional energy cone model, the inclusion of *branch* energy cones is able to increase the maximum runout distance from <2.0 to ~4.0 km in the directions of preferential channelization (i.e., SW and E), where we arbitrarily choose the isoline 0.5 as a reference inundation polygon (Figures 4b and 4c for comparison), whereas minor modifications are produced in the inundation area toward N. In terms of channelization directions, results are consistent with the dispersal of PDC deposits produced during the 2008–2009 Chaitén eruption (Lara, 2009; Major & Lara, 2013), where the transport of PDCs occurred preferentially in two of the directions characterized by high runout distances in numerical simulations: SW and N (Figures 4a and 4b). We highlight that, using the traditional energy cone model, large runout distances toward SW and E (e.g., ~4.0 km for the reference isoline 0.5) require a slope of the energy cones (i.e., $\tan(\varphi)$) of 0.25–0.35, producing probability maps characterized by high runout distances also in directions where channelization is not expected to occur (Figures 4a and 4d for comparison). Even if results presented in Figure 4 underestimate the runout distance toward SW when they are compared with the February 2009 deposits, we remark that these simulations, which clearly show the channelization effect of the branching formulation, were not performed to fit the inundation polygon of the 2008–2009 PDC deposits, which is instead performed and discussed in Figure 5 and below in this section.

Figures 4e and 4f present the evolution of the normalized values of inundation area and runout distance (i.e., with respect to the final values of each simulation) during the construction of the different orders of energy

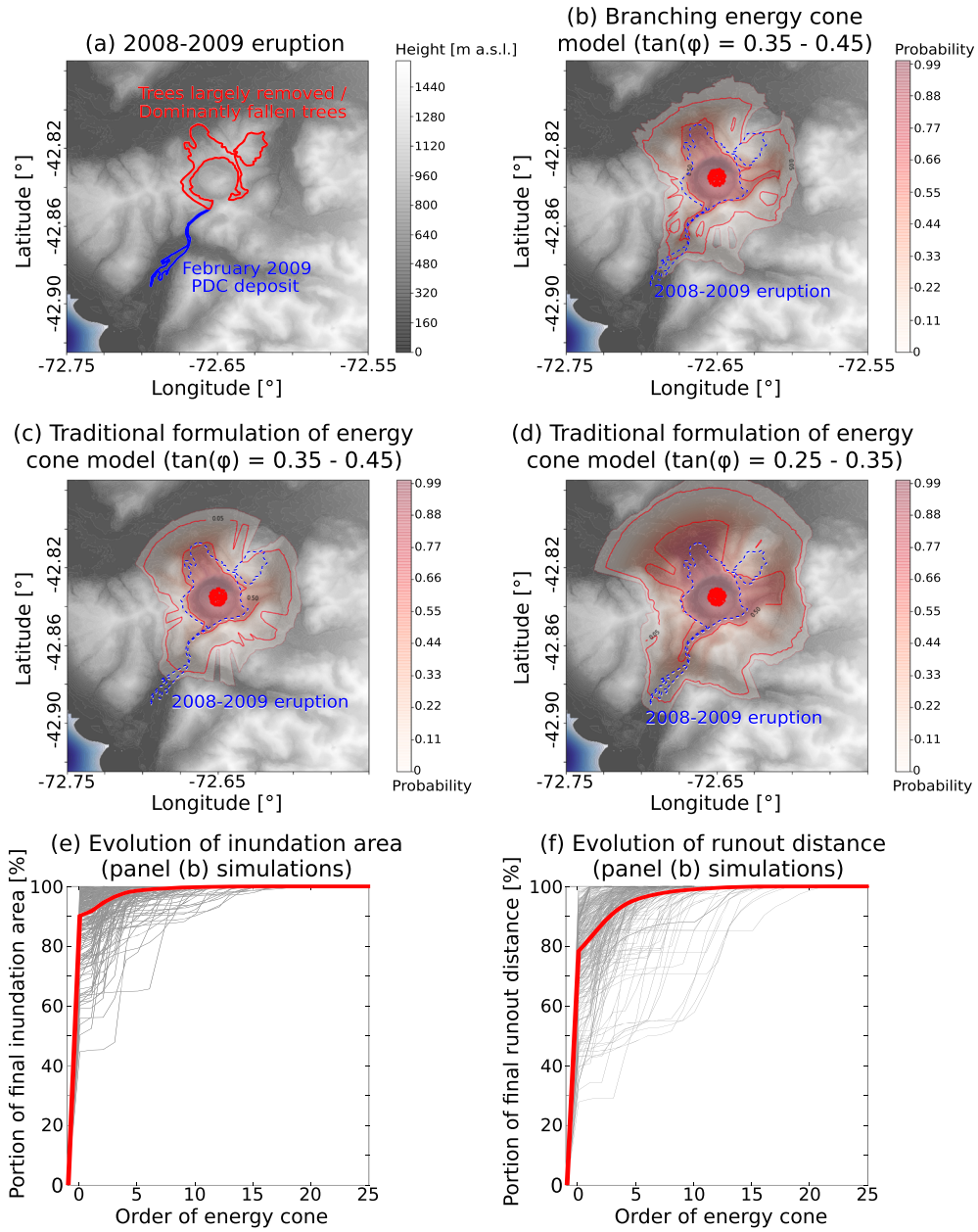

Figure 4. (a) Deposits associated with the 2008–2009 Chaitén eruption. Modified from Major et al. (2013). (b) Probability map related to a set of simulations ($N = 300$) performed by adopting the branching energy cone model. (c and d) Probability maps related to two sets of simulations ($N = 300$) performed by adopting the traditional energy cone model. (e and f) Normalized inundation area and normalized runout distance (i.e., with respect to the modeled, final values) reported as a function of the order of the energy cones, for panel (b) simulations. Input parameters are presented in Table S1.

cones for the simulations presented in Figure 4b. Most simulations require the construction of more than 10 orders of energy cones, but 5 orders of energy cones are enough to reach >95% of the final, modeled inundation area and runout distance. However, in some cases, high-order energy cones are able to modify significantly the runout distance. In Tables S1–S4 we present some metrics to compare the output inundation polygons derived from these and other sets of simulations, including the statistics of inundation area, maximum (R_{max}) and minimum (R_{min}) runout distance, R_{max}/R_{min}, and r_c, defined as the ratio of the square root of inundation area and the product between R_{max} and $\sqrt{\pi}$. These results

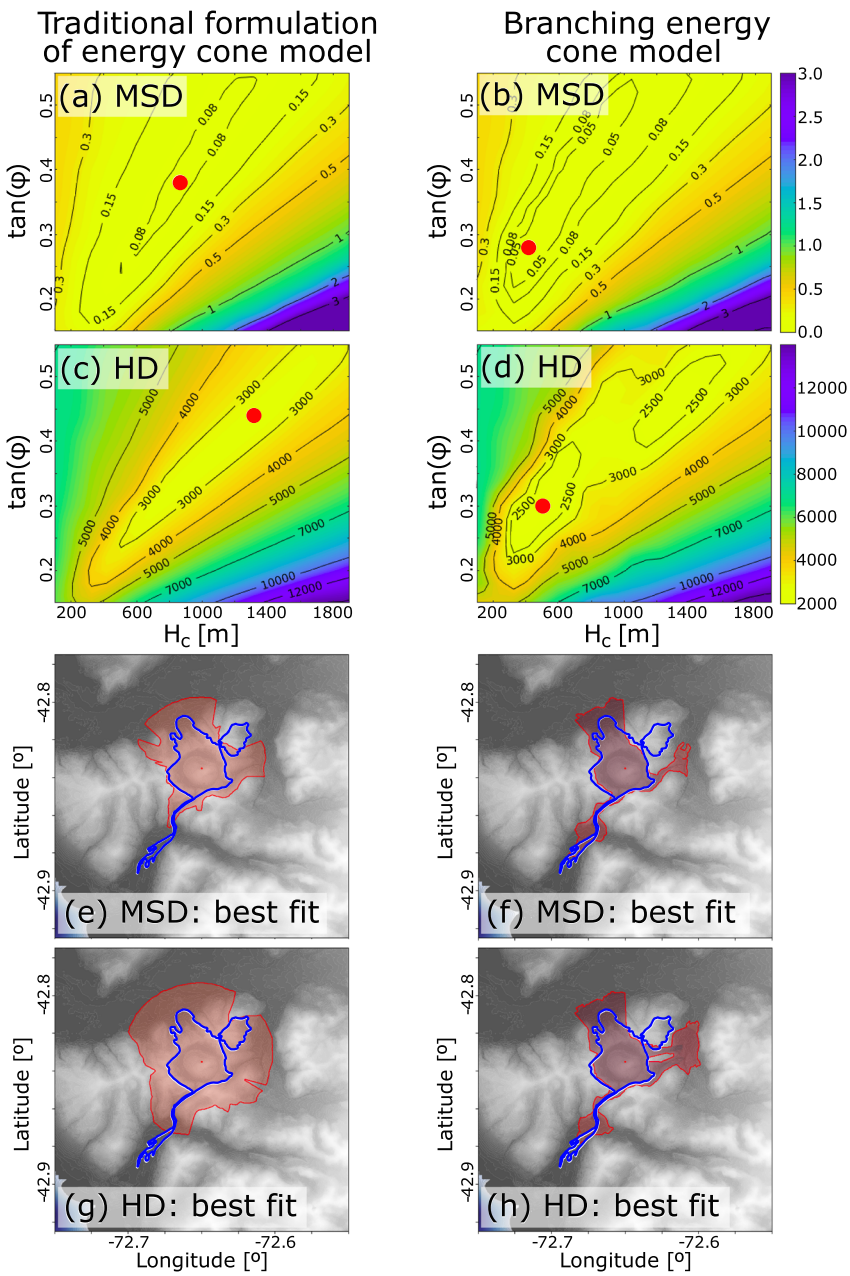

Figure 5. (a–d) Contour plots of MSD (a and b) and Hausdorff distance (HD, c and d) as a function of H_c and tan(φ) for a set of simulations performed using the traditional (a and c) and branching (b and d) energy cone models, considering PDC deposits associated with the 2008–2009 Chaitén eruption. MSD and HD are parameters able to quantify the coincidence degree between modeled and observed inundation polygons. The lower these parameters, the higher the coincidence degree between the inundation zones. The red points represent the best fit positions obtained in each case. (e–h) Inundation maps associated with the best fit conditions presented in panels (a)–(d), and their comparison with the reference PDC deposit (2008–2009 Chaitén eruption; see Tables S1 and S2).

highlight that the branching formulation usually translates in significant differences in runout distance-based parameters (e.g., R_{max}/R_{min} or r_c), while inundation area modifications derived from the introduction of high-order energy cones tend to be moderate.

Although the pyroclastic flow deposits derived from the 2008–2009 Chaitén eruption were formed by different collapse events and thus their generation/propagation conditions were different (column and dome

collapse), we applied different methodologies to compare the real deposit and the modeled inundation polygons. A simple comparison can be performed by computing the mean square distance between the different border points of each inundation polygon and the nearest bound of the other one, normalized by the square of the mean runout distance measured from the real deposit. The lower this parameter, hereafter MSD (mean square distance), the higher the coincidence degree between the inundation zones. Figures 5a and 5b show MSD as a function of H_c and $\tan(\varphi)$ for a set of simulations performed using the traditional and branching energy cone models, considering the PDC deposits associated with the 2008–2009 Chaitén eruption to compute MSD. Results indicate that the branching formulation reduces significantly the minimum MSD (from 0.072 to 0.027) and expands the zone of the pairs (H_c, $\tan(\varphi)$) able to produce low values of MSD (e.g., for the variation range considered here for input parameters, the surface associated with values of MSD lower than 0.08 increases by a factor of ~2.8). Figures 5e and 5f present the inundation areas associated with both best fit conditions (Tables S1 and S2), showing clearly that the branching formulation fits better the PDC deposits of this eruption.

Other useful parameter to compare inundation polygons is the Hausdorff distance (HD), which represents the maximum distance between the overestimated and underestimated sectors of the modeled polygon, when compared with the real deposit:

$$HD = \max\left\{ \max_{a \in A}\left(\min_{b \in B}\left(d(a,\, b)\right)\right), \max_{b \in B}\left(\min_{a \in A}\left(d(a,\, b)\right)\right)\right\} \tag{21}$$

where A and B are the curves that represent the external bounds of the polygons.

Figures 5c and 5d present the Hausdorff distance for a set of simulations performed using the traditional and branching energy cone formulations, considering the deposits associated with the 2008–2009 Chaitén eruption to compute this parameter. The branching formulation is able to reduce the minimum HD from 2,612 to 2,060 m, showing results consistent with those obtained using MSD. Figures 5g and 5h present the inundation polygons derived from both best fit conditions (Table S2), showing again that the branching energy cone model fits better the reference polygon. We highlight that we only consider distance-based comparison parameters because, in general, inundation area-based comparison parameters, such as the Jaccard similarity coefficient, are less sensitive to the channelization effect of branching models. This is because significant channelization zones tend to be relatively narrow, which is particularly evident for the 2008–2009 Chaitén eruption (e.g., the inundation area associated with the February 2009 PDC represents less than 8% of the total inundation zone).

To compare the sensitivity of both formulations with respect to H_c, we performed a set of simulations with variable values of H_c ($0 - 1200$ m above topography), fixed conditions for φ ($\tan(\varphi) = 0.4$), and slightly variable coordinates for the source position ($P_{0,0} = (-72.650°, -42.835°)$, considering a 200 m radius variability zone). Figures 6a and 6c present the relationship between runout distance in specific directions (toward E and SW) and inundation area, highlighting the ability of the strategy presented here to model the channelization of pyroclastic material, with runout distances significantly higher than that observed with the traditional formulation. Results highlight the strong control of caldera limits in numerical results, with runout distances higher than 3.5 and 4.0 km toward E and SW, respectively, for all the simulations able to overcome the caldera border. Otherwise, runout distance rarely exceeds 2.0 km. This effect is not observed in the results associated with the traditional energy cone model, where runout distance presents a gradual increase as the inundation area increases (Figures 6a and 6c). On the other hand, the relationship between runout distance in specific directions and H_c is presented in Figures 6b and 6d, where we can note that the dependence of runout distance on H_c is significantly reduced by considering the branching energy cone model instead of the traditional formulation. Indeed, for simulations that overcome caldera limits, the ratio between variations of runout distance toward E and H_c is reduced from ~2.8 to ~1.2, while the ratio between variations of runout distance toward SW and H_c is reduced from ~3.2 to ~0.8. It is also important to note that no major differences are observed in the dependence between inundation area and H_c when the traditional and branching formulations of the energy cone model are compared.

In order to compare the results of the formulation presented here with a model based on the shallow-water equations, we adopted the code IMEX_SfloW2D (de' Michieli Vitturi et al., 2019). IMEX_SfloW2D requires

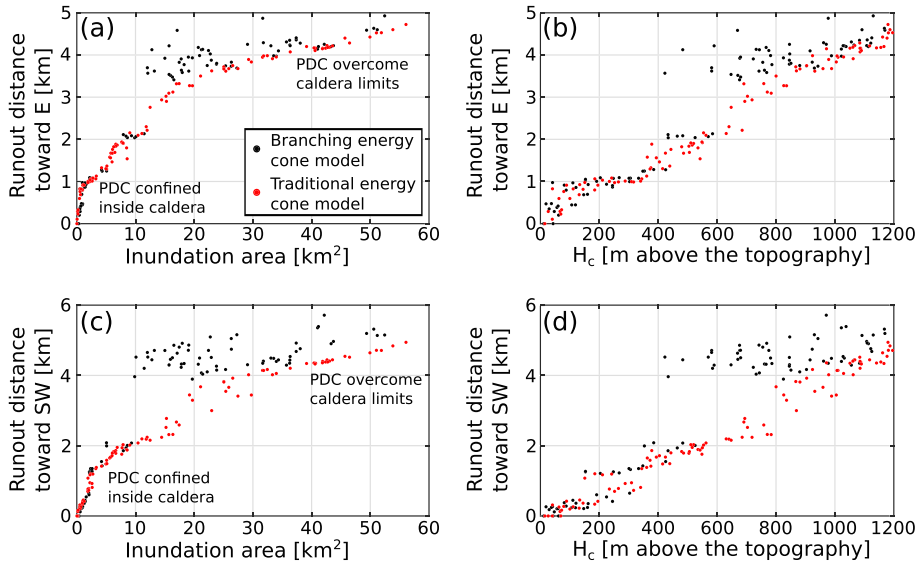

Figure 6. (a and b) Runout distance toward E reported as a function of inundation area (a) and H_c (b), for simulations associated with the traditional and branching energy cone models. (c and d) Runout distance toward SW reported as a function of inundation area (c) and H_c (d), for simulations associated with the traditional and branching energy cone models. These simulations were performed considering the Chaitén volcano topography, using variable values of H_c, fixed conditions for φ, and slightly variable coordinates for the collapse position.

additional input parameters with respect to the energy cone model such as the volume of collapsing material, which may hinder the development of comparisons between both models. For obtaining comparable results, we performed a set of simulations with IMEX_SfloW2D by adopting fixed conditions for the collapsing material rheology (Voellmy-Salm model with $\mu = 0.4$ and $\xi = 5 \cdot 10^6$ m/s^2, in order to avoid the viscous turbulent friction and induce a linear dissipation law), and the collapsing volume defined as a cylinder extended from the surface to an altitude of 1,500 m a.s.l., with a variable basal radius (R) between 100 and 400 m. These simulations were compared with the results of a set of simulations performed by adopting the branching energy cone model, considering $\tan(\varphi) = 0.4$, $H_c = 1{,}500$ m a. s. l., and expected source coordinates coincident with the center of the collapsing cylinders adopted in IMEX_SfloW2D, using a variability zone defined by a circle with a radius of 200 m. Results show a strong agreement between the inundation areas predicted by both models (Figures 7a and 7b and Table S2), with three zones of preferential channelization (N, E, and SW) and runout distances between ~3.5 and ~5.0 km, while the traditional energy cone formulation is unable to model high runout distances toward SW (Figure 7c and Table S2). The simulations performed with the branching energy cone model ($N = 300$ simulations) took ~2,500 s on an Intel Core i7-4510U CPU at 2.00 GHz (i.e., <10 s per simulation), while each IMEX_SfloW2D simulation took ~2,000 s. This highlights the low computational cost associated with the formulation proposed here, allowing a rapid use even in absence of large computational power.

Finally, the results associated with a test simulation on Citlaltépetl volcano are presented in Figure 8a (Table S3), which were compared with the inundation maps presented by Sheridan et al. (2004), where a block-and-ash-flow with runout distance of 10–13 km (Figure 8b) was considered as a reference case study. Results highlight that, for Citlaltépetl volcano, the extent of the inundation area is strongly controlled by the volcano topography, as suggested by Sheridan et al. (2004). In this case, because of the particularly large elevation difference between volcano crater and the surrounding valleys, numerical modeling suggests that PDCs are able to cover vast areas and to produce high runout distances. Indeed, for the input conditions considered here, most of the simulations (>70%) present runout distances between 8 and 14 km, with largely variable inundation areas (between 40 and 120 km^2), and two preferential transport directions: SE and NNE. These results are in agreement with those obtained by using the model FLOW3D, and they differ from the inundation area provided by the traditional energy cone model (Figures 8a and 8b; Sheridan et al., 2004),

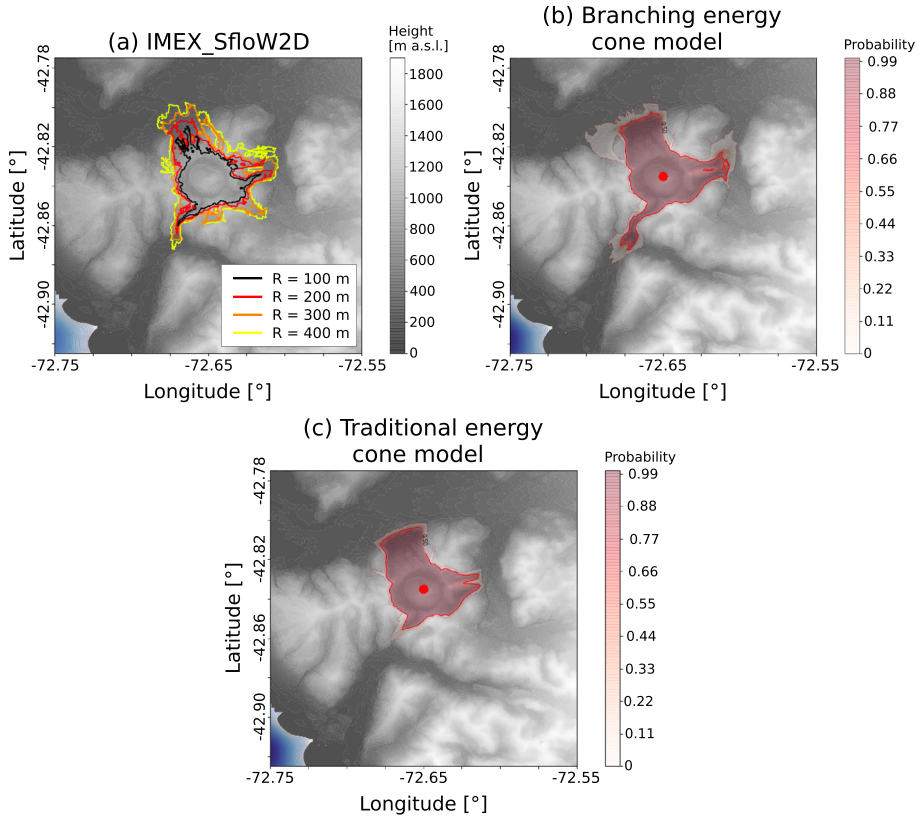

Figure 7. (a) Inundation area of PDCs related to four simulations performed with IMEX_SfloW2D. In these simulations, the collapsing volume is defined as a cylinder extended from the surface to an altitude of 1,500 m a.s.l., with R as its basal radius (see legend). (b and c) Probability maps of inundation area of PDCs related to two sets of simulations ($N = 300$) performed with the branching and traditional energy cone model, respectively. Input parameters are presented in Table S2.

which envelopes the footprint derived from FLOW3D simulations and overestimates the inundation area in high-elevation zones.

3.2. Branching Box Model

Figure 9a presents the inundation map associated with a set of simulations ($N = 300$) performed for Chaitén volcano (Chile) by adopting the branching box model, where we consider specific variation ranges for the input parameters (Table S4), which allow to capture a wide set of PDC formation/propagation conditions. Figure 9b presents the equivalent results associated with the traditional box model (i.e., only considering the *root* conoid). In this case, the inclusion of *branch* conoids increases the maximum runout distance from <2.0 to >4.0 km in the directions of preferential flow channelization (i.e., N, SW, and E, Figures 9a and 9b), where we have adopted the isoline 0.5 as an arbitrary reference inundation polygon. In terms of channelization directions, these results are consistent with the deposits produced during the 2008–2009 Chaitén eruption (Figures 4a and 9a; Lara, 2009; Major et al., 2013). Conversely, using the traditional box model, large runout distances toward N, SW, and E (e.g., >4.0 km for the reference isoline 0.5) require a significantly larger collapsing volume, generating inundation maps characterized by high runout distances in directions where channelization processes are not expected to occur (e.g., NW and SE; Figures 9a and 9d). In any case, we remark that numerical results derived from the application of the two branching models presented here do not suggest a significant inundation probability toward NE, which is not in agreement with a portion of the deposits of the 2008–2009 eruption (Figures 4 and 9). Major and Lara (2013) reported that this PDC was generated during the explosive phase of the eruption, presumably derived from column collapse processes (in particular, on 2 May 2008, when the eruptive column reached ~20 km height). We suggest that its provenience from a well-developed eruptive column could explain that this PDC was less affected by the caldera

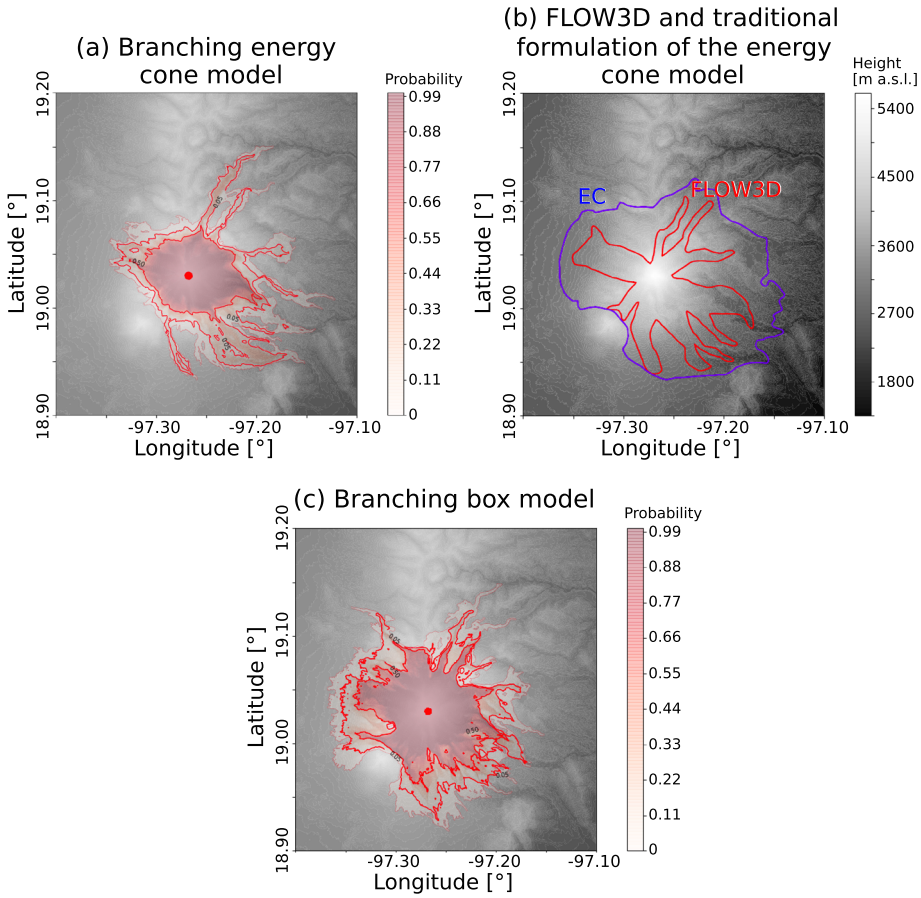

Figure 8. (a) Probability map related to a set of test simulations performed for Citlaltépetl volcano (branching energy cone model; $P_{0,0} = (-97.268°, 19.030°)$, considering a 300 mradius variability zone, $H_c = 300 - 500$ m above topography, and $\tan(\varphi) = 0.40 - 0.50$; see Table S3). (b) PDC hazard map in Citlaltépetl volcano, using FLOW3D and the traditional energy cone model (EC). The input parameters used in these simulations are supposed to describe the deposits associated with a specific block-and-ash flow (4,000 years BP). Modified from Sheridan et al. (2004). (c) Probability map related to a set of test simulations performed for Citlaltépetl volcano (branching box model; $P_{0,0} = (-97.268°, 19.030°)$, considering a 300 m radius variability zone, $V_{0,0} = 8 \cdot 10^8 - 1.2 \cdot 10^9$ m^3, $\phi_{0(0,0)} = 0.005 - 0.015$, $w_s = 0.2 - 1.0$ m/s, $Fr = 1.0 - 1.2$, $\rho_p = 800 - 1{,}000$ kg/m^3, and $\rho_a = 0.9 - 1.1$ kg/m^3; see Table S4).

topography in the NE flank, in contrast to that observed in our simulations, where the source point is located in the central region of the caldera. We stress that PDCs generated during the dome-forming phase, derived from dome collapse and likely affected by caldera topography, were instead preferentially channelized through a caldera creek and the Chaitén River Valley (Figure 4a) when they overcame the SW caldera limit (Major & Lara, 2013), as shown by numerical results.

Figures 9e and 9f present the evolution of the normalized values of inundation area and runout distance (i.e., with respect to the final values) during the construction of the different orders of conoids for the simulations presented in Figure 9a. Most simulations need the construction of more than 20 orders of conoids, but 10 orders of conoids are enough to reach >95% of the final, modeled inundation area. However, high-order conoids are able to modify significantly the resulting runout distance.

The results related to a test simulation performed for Citlaltépetl volcano are described in Figure 8c (Table S4). In this case, the inundation area is less controlled by the topography (Figures 8a and 8c for comparison), and the modeled PDC is not able to develop important channelization processes. With the input conditions considered here, most of the simulations (>80%) present runout distances between 8 and 12 km, and inundation areas between 70 and 220 km^2. The parameter r_c (i.e., ratio of the square root of

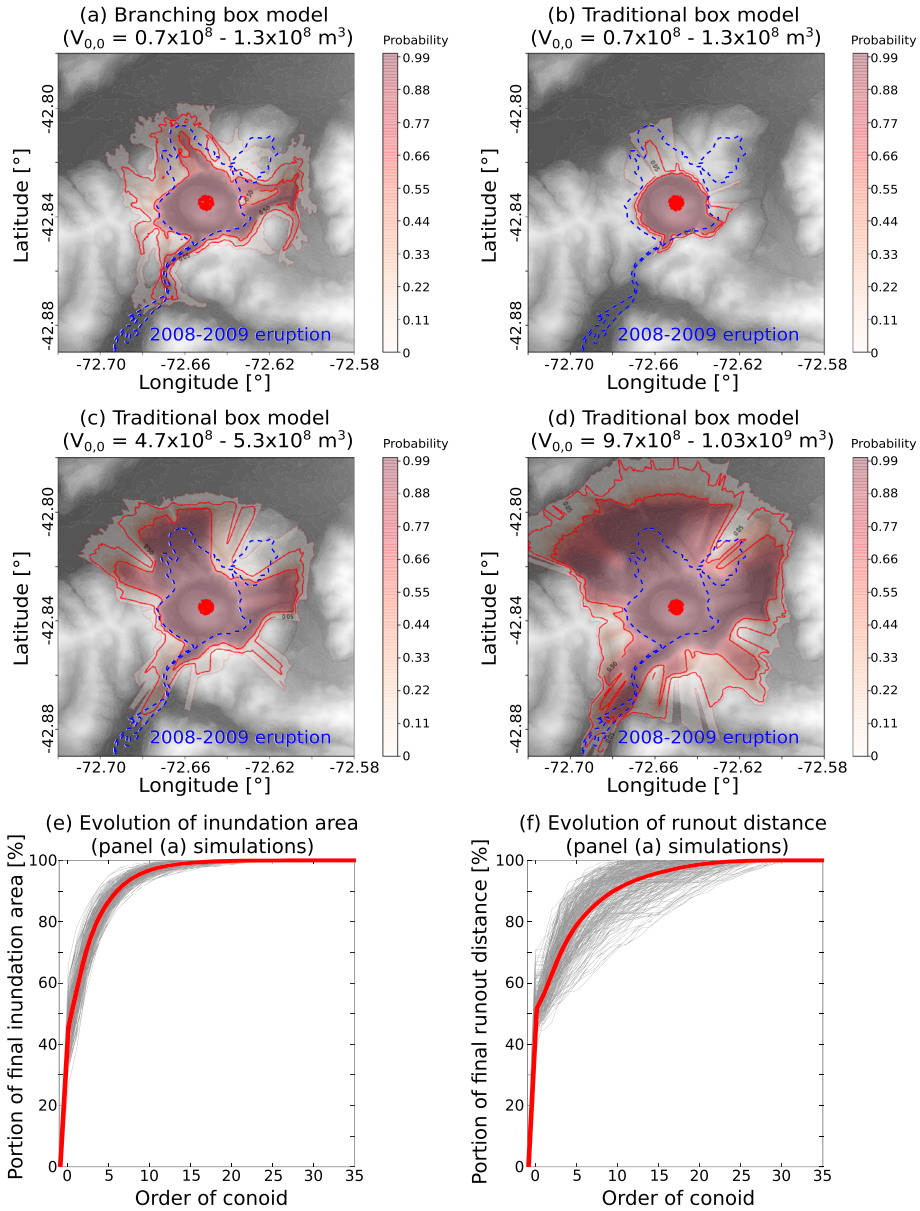

Figure 9. (a) Probability map related to a set of simulations ($N = 300$) performed by adopting the branching box model. (b–d) Probability maps related to three sets of simulations ($N = 300$) performed by adopting the traditional box model, and using different collapsing volumes. (e and f) Normalized inundation area and normalized runout distance (i.e., with respect to the modeled, final values) reported as a function of the order of the conoids, for panel (a) simulations. Input parameters are presented in Table S4.

inundation area and the product between $\sqrt{\pi}$ and R_{max}) is a useful metric for highlighting the weak channelization of pyroclastic material observed in this case. The higher the value of r_c, which ranges between 0 and 1, the weaker the channelization of pyroclastic material (some illustrative examples are presented in Figure S2). For the set of simulations presented in Figure 8c (i.e., with the branching box model), the mean value of r_c is 0.63 with 90% of the simulations ranging between 0.56 and 0.68, while the simulations associated with the branching energy cone model (Figure 8a) present significantly lower results for this parameter, with a mean value of 0.43 and 90% of the simulations ranging between 0.33 and 0.59. This difference can be also observed by considering R_{max}/R_{min}, which tends to be higher for intense channelization processes. In the simulations presented in Figure 8c (i.e., with the branching box model),

this parameter ranges from 2.3 to 3.3 (mean value of 2.7), while it ranges between 2.2 and 9.4 in the branching energy cone model simulations (mean value of 4.7; Tables S3 and S4).

4. Discussion

The branching technique is a general methodology, applicable to any PDC model able to describe the dissipation of kinetic energy with distance. We have illustrated its implementation by applying it to the energy cone and the box model. However, the two models have different applicability fields to volcanological problems and their use should be performed critically. Here we summarize the main constraints and limitations of both approaches.

The energy cone model describes the kinetic energy evolution of a frictional flow (having constant friction parameter). It is more suited to dense granular flows, whose dynamics is dominated by frictional stress and the longitudinal component of gravity acceleration (Campbell, 2006; Pudasaini & Domnik, 2009). For this reason, concentrated currents are also more affected by the local topography and by the volcano slope. Although there is a huge debate (e.g., Lucas et al., 2014; Pudasaini & Hutter, 2007) about the possibility of describing rapid granular avalanches (including pyroclastic flows; Charbonnier & Gertisser, 2012) with a constant and shear-independent friction model, the energy cone model presents many applications to relatively small-scale PDCs, especially when they are confined within the topography of the volcanic edifice and propagate over steep slopes.

On the other hand, the box model describes the kinematics (i.e., the front speed and average thickness and particle concentration) of inertial pyroclast-laden gravity currents. In contrast to the energy cone, this model assumes that friction is negligible and thus the flow dynamics is driven by the hydrostatic pressure contrast, while particle sedimentation dissipates momentum. Effects associated with steep slopes are typically nonhydrostatic, so that the box model formulation is strictly valid for low average slopes. It is worth reminding that inertial currents are not necessarily dilute flows (several fluidization processes can strongly reduce granular friction in natural granular flows), and in particular, low aspect ratio ignimbrites (Walker, 1983) are expected to be dominantly inertial. Channelization phenomena are therefore expected to be stronger in dominantly concentrated, frictional PDCs (or in their concentrated, basal part), but topography can affect inertial density currents as well, as demonstrated in the laboratory (Woods et al., 1998), in numerical simulations (Giordano & Dobran, 1994; Todesco et al., 2006) and in nature (Cas et al., 2011).

Both the presented test cases, like most of natural PDCs, are in our view intermediate between dominantly frictional and dominantly inertial flows. For example, while the proximal dynamics of PDCs at Chaitén volcano was likely dominated by propagation on steep slopes, the entrance in the Chaitén River Valley, characterized by gentler slopes, was probably dominated by hydraulic effects. However, these hypotheses are beyond the scope of the present paper, whose aim is to present a general methodology to improve any kinetic model for PDCs. In fact, here we have demonstrated that the new methodology enhances the two tested models, better describing channelization effects on a three-dimensional topography and reducing model sensitivity to unconstrained input parameters when topography controls PDC propagation. These two improvements are of paramount importance for hazard assessment studies.

5. Conclusions

The traditional formulation of kinetic models is not able to properly consider the occurrence of channelization processes of pyroclastic material and thus it tends to underestimate the runout distance into channels (e.g., Sandri et al., 2018), which limits strongly its applicability in volcanic hazard assessment studies. To address this point, here we have described a new strategy to adapt kinetic models, like the energy cone and the box model, to consider the effects of channelization processes during the propagation of PDCs over a rugged topography. This strategy consists in modeling secondary collapse processes (represented by secondary conoids) in the expected zones of flow channelization, adopting a tree branch-like structure and appropriate assumptions for setting the properties of the secondary sources. The characteristics of these secondary sources are based on the redistribution of a key physical variable such as energy or flow mass, depending on the adapted kinetic model.

This branching strategy was implemented by adapting the two most widely used kinetic models: the energy cone (e.g., Malin & Sheridan, 1982; Ogburn & Calder, 2017) and the box model (e.g., Esposti Ongaro et al., 2016; Huppert & Simpson, 1980). These models have been applied to describe PDCs derived from column and dome collapse processes and their appropriateness depends on the properties of the specific flow investigated (frictional granular flows vs. inertial turbulent PDCs, as discussed above). Although these models differ in their hypotheses and formulations, they can be recast to a common mathematical framework to which our new modeling methodology has been applied. We remark that the proposed methodology does not require the inclusion of additional, poorly constrained input parameters, and the low computational cost associated with these codes allows to adopt a probabilistic approach in volcanic hazard assessment (Bevilacqua et al., 2017; Neri, Bevilacqua, et al., 2015; Sandri et al., 2018; Tierz, Sandri, Costa, Sulpizio, et al., 2016). This approach permits to consider the natural variability of the eruptive process by sampling model input parameters within the expected variation ranges and running a large set of simulations, while numerical results are studied on the *ensemble* of simulations.

The implementation of the branching strategy, illustrated considering two case studies (Chaitén and Citlaltépetl volcanoes), has a significant impact on the resulting inundation maps. In some case studies, both the branching energy cone and the branching box model are able to increase the maximum runout distance in channelized zones by a factor of ~2.0 in comparison with their traditional formulations, with important consequences for PDC hazard assessment. In fact, this formulation enhances the capability of kinetic models to consider topographic effects in PDC transport dynamics and increases the model performance to simulate channelization processes and reproduce real pyroclastic deposits. The improvement in the accuracy of modeling results has been evidenced by different distance-based parameters able to measure the similarity degree between simulated inundation maps and real pyroclastic deposits, such as the Hausdorff distance and the mean square distance, which are significantly reduced by adopting the branching formulations instead of the traditional ones. Importantly, the results associated with the branching energy cone model are significantly less controlled by the source height (H_c), in comparison with the traditional formulation. Because of the intrinsic difficulties to properly constrain this parameter, this represents a further, relevant strength of this strategy for application purposes. Finally, we remark that branching energy cone model results are also consistent with other numerical tools, such as FLOW3D (Sheridan et al., 2004) and IMEX_SfloW2D (de' Michieli Vitturi et al., 2019).

All in all, we suggest that these models can represent a useful tool for the early assessment of volcanic hazard at poorly documented volcanoes and the construction of hazard maps, as they highlight the topographic control on PDC propagation by modeling channelization processes, involve low computational costs, and reduce the sensitivity of kinetic models to poorly constrained source conditions. In this way, this formulation makes kinetic models a more robust tool for volcanic hazard assessment.

Data Availability Statement

The models used in this paper are available in https://github.com/AlvaroAravena/ECMapProb and https://github.com/AlvaroAravena/BoxMapProb and also in the repository associated with the following DOI: 10.5281/zenodo.3755086.

Acknowledgments
We thank Pablo Tierz and Sylvain Charbonnier for their suggestions and comments. This research has been supported by the Italian Ministry of University and Research through the FISR project "Sale Operative Integrate e Reti di Monitoraggio del Futuro".

References

Alberico, I., Lirer, L., Petrosino, P., & Scandone, R. (2002). A methodology for the evaluation of long-term volcanic risk from pyroclastic flows in Campi Flegrei (Italy). *Journal of Volcanology and Geothermal Research*, *116*(1–2), 63–78. https://doi.org/10.1016/S0377-0273(02)00211-1

Asmussen, S., & Hering, H. (1983). *Branching processes*. Boston: Springer. https://doi.org/10.1007/978-1-4615-8155-0

Aspinall, W.P., Bevilacqua, A., Costa, A., Inakura, H., Mahony, S., Neri, A., & Sparks, S. (2019), Probabilistic reconstruction (or forecasting) of distal runouts of large magnitude ignimbrite PDC flows sensitive to topography using mass-dependent inversion models, paper presented at AGU Fall Meeting Abstracts.

Auker, M., Sparks, R., Siebert, L., Crosweller, H., & Ewert, J. (2013). A statistical analysis of the global historical volcanic fatalities record. *Journal of Applied Volcanology*, *2*(1), 2. https://doi.org/10.1186/2191-5040-2-2

Belousov, A., Voight, B., & Belousova, M. (2007). Directed blasts and blast-generated pyroclastic density currents: A comparison of the Bezymianny 1956, Mount St Helens 1980, and Soufrière Hills, Montserrat 1997 eruptions and deposits. *Bulletin of Volcanology*, *69*(7), 701–740. https://doi.org/10.1007/s00445-006-0109-y

Bevilacqua, A. (2016). *Doubly stochastic models for volcanic hazard assessment at Campi Flegrei caldera*. Pisa: Springer. https://doi.org/10.1007/978-88-7642-577-6

Bevilacqua, A. (2019), Notes on the analytic solution of box model equations for gravity-driven particle currents with constant volume, *arXiv preprint arXiv:1903.08582*.

Bevilacqua, A., Neri, A., Bisson, M., Esposti Ongaro, T., Flandoli, F., Isaia, R., et al. (2017). The effects of vent location, event scale, and time forecasts on pyroclastic density current hazard maps at Campi Flegrei caldera (Italy). *Frontiers in Earth Science*, *5*, 72. https://doi.org/10.3389/feart.2017.00072

Biagioli, G., Bevilacqua, A., Esposti Ongaro, T., & de' Michieli Vitturi, M. (2019). PyBox: A Python tool for simulating the kinematics of Pyroclastic density currents with the box-model approach Reference and User's Guide.

Bonnecaze, R., Hallworth, M., Huppert, H., & Lister, J. (1995). Axisymmetric particle-driven gravity currents. *Journal of Fluid Mechanics*, *294*, 93–121. https://doi.org/10.1017/S0022112095002825

Branney, M., & Kokelaar, P. (2002). Pyroclastic density currents and the sedimentation of ignimbrites, Geological Society of London.

Campbell, C. (2006). Granular material flows–an overview. *Powder Technology*, *162*(3), 208–229. https://doi.org/10.1016/j.powtec.2005.12.008

Carn, S., Pallister, J., Lara, L., Ewert, J., Watt, S., Prata, A., et al. (2009). The unexpected awakening of Chaitén volcano, Chile, *EOS. Transactions of the American Geophysical Union*, *90*(24), 205–206. https://doi.org/10.1029/2009EO240001

Cas, R. A., Wright, H., Folkes, C., Lesti, C., Porreca, M., Giordano, G., & Viramonte, J. (2011). The flow dynamics of an extremely large volume pyroclastic flow, the 2.08-Ma Cerro Galán Ignimbrite, NW Argentina, and comparison with other flow types. *Bulletin of Volcanology*, *73*(10), 1583–1609. https://doi.org/10.1007/s00445-011-0564-y

Charbonnier, S., & Gertisser, R. (2011). Deposit architecture and dynamics of the 2006 block-and-ash flows of Merapi Volcano, Java, Indonesia. *Sedimentology*, *58*(6), 1573–1612. https://doi.org/10.1111/j.1365-3091.2011.01226.x

Charbonnier, S., & Gertisser, R. (2012). Evaluation of geophysical mass flow models using the 2006 block-and-ash flows of Merapi Volcano, Java, Indonesia: Towards a short-term hazard assessment tool. *Journal of Volcanology and Geothermal Research*, *231*, 87–108.

Cole, P., Neri, A., & Baxter, P. (2015). Hazards from pyroclastic density currents, in *The encyclopedia of volcanoes* (pp. 943-956). New York: Elsevier.

Dade, W., & Huppert, H. (1996). Emplacement of the Taupo ignimbrite by a dilute turbulent flow. *Nature*, *381*(6582), 509–512. https://doi.org/10.1038/381509a0

de' Michieli Vitturi, M., Esposti Ongaro, T., Lari, G., & Aravena, A. (2019). IMEX_SfloW2D 1.0: a depth-averaged numerical flow model for pyroclastic avalanches. *Geoscientific Model Development*, *12*(1), 581–595.

Dioguardi, F., & Mele, D. (2018). PYFLOW_2. 0: A computer program for calculating flow properties and impact parameters of past dilute pyroclastic density currents based on field data. *Bulletin of Volcanology*, *80*(3), 28. https://doi.org/10.1007/s00445-017-1191-z

Druitt, T. (1998). Pyroclastic density currents, *Geological Society* (Vol. 145(1), pp. 145–182). London: Special Publications. https://doi.org/10.1144/GSL.SP.1996.145.01.08

Dufek, J., Esposti Ongaro, T., & Roche, O. (2015). Pyroclastic density currents: Processes and models. In *The encyclopedia of volcanoes* (pp. 617–629). New York: Elsevier.

Esposti Ongaro, T., Cavazzoni, C., Erbacci, G., Neri, A., & Salvetti, M. (2007). A parallel multiphase flow code for the 3D simulation of explosive volcanic eruptions. *Parallel Computing*, *33*(7–8), 541–560. https://doi.org/10.1016/j.parco.2007.04.003

Esposti Ongaro, T., Komorowski, J., de' Michieli Vitturi, M., & Neri, A. (2019). Computer simulation of explosive eruption scenarios at La Soufrière de Guadeloupe (FR): Implications for volcanic hazard assessment, paper presented at AGU Fall Meeting Abstracts.

Esposti Ongaro, T., Orsucci, S., & Cornolti, F. (2016). A fast, calibrated model for pyroclastic density currents kinematics and hazard. *Journal of Volcanology and Geothermal Research*, *327*, 257–272. https://doi.org/10.1016/j.jvolgeores.2016.08.002

García, O., Martí, J., Aguirre, G., Geyer, A., & Iribarren, I. (2011). Pyroclastic density currents from Teide–Pico Viejo (Tenerife, Canary Islands): Implications for hazard assessment. *Terra Nova*, *23*(3), 220–224. https://doi.org/10.1111/j.1365-3121.2011.01002.x

Giordano, G., & Dobran, F. (1994). Computer simulations of the Tuscolano Artemisio's second pyroclastic flow unit (Alban Hills, Latium, Italy). *Journal of Volcanology and Geothermal Research*, *61*(1–2), 69–94. https://doi.org/10.1016/0377-0273(94)00013-1

Gladstone, C., & Woods, A. (2000). On the application of box models to particle-driven gravity currents. *Journal of Fluid Mechanics*, *416*, 187–195. https://doi.org/10.1017/S0022112000008879

Gurioli, L., Sulpizio, R., Cioni, R., Sbrana, A., Santacroce, R., Luperini, W., & Andronico, D. (2010). Pyroclastic flow hazard assessment at Somma–Vesuvius based on the geological record. *Bulletin of Volcanology*, *72*(9), 1021–1038. https://doi.org/10.1007/s00445-010-0379-2

Haccou, P., Jagers, P., & Vatutin, V. (2005). *Branching processes: Variation, growth, and extinction of populations*. Cambridge: Cambridge University Press. https://doi.org/10.1017/CBO9780511629136

Hallworth, M., Hogg, A., & Huppert, H. (1998). Effects of external flow on compositional and particle gravity currents. *Journal of Fluid Mechanics*, *359*, 109–142. https://doi.org/10.1017/S0022112097008409

Harris, T. (1963). *The theory of branching processes*. Berlin Heidelberg: Springer-Verlag. https://doi.org/10.1007/978-3-642-51866-9

Hayashi, J., & Self, S. (1992). A comparison of pyroclastic flow and debris avalanche mobility. *Journal of Geophysical Research*, *97*(B6), 9063–9071. https://doi.org/10.1029/92JB00173

Hsu, K. (1975). Catastrophic debris streams (sturzstroms) generated by rockfalls. *Geological Society of America Bulletin*, *86*(1), 129–140. https://doi.org/10.1130/0016-7606(1975)86%3C129:CDSSGB%3E2.0.CO;2

Huppert, H., & Simpson, J. (1980). The slumping of gravity currents. *Journal of Fluid Mechanics*, *99*(4), 785–799. https://doi.org/10.1017/S0022112080000894

Kelfoun, K. (2011). Suitability of simple rheological laws for the numerical simulation of dense pyroclastic flows and long-runout volcanic avalanches. *Journal of Geophysical Research*, *116*, B08209. https://doi.org/10.1029/2010JB007622

Kelfoun, K., Samaniego, P., Palacios, P., & Barba, D. (2009). Testing the suitability of frictional behaviour for pyroclastic flow simulation by comparison with a well-constrained eruption at Tungurahua volcano (Ecuador). *Bulletin of Volcanology*, *71*(9), 1057–1075. https://doi.org/10.1007/s00445-009-0286-6

Komorowski, J., Jenkins, S., Baxter, P., Picquout, A., Lavigne, F., Charbonnier, S., et al. (2013). Paroxysmal dome explosion during the Merapi 2010 eruption: Processes and facies relationships of associated high-energy pyroclastic density currents. *Journal of Volcanology and Geothermal Research*, *261*, 260–294. https://doi.org/10.1016/j.jvolgeores.2013.01.007

Lara, L. (2009). The 2008 eruption of the Chaitén Volcano, Chile: A preliminary report. *Andean Geology*, *36*(1), 125–129.

Lucas, A., Mangeney, A., & Ampuero, J. (2014). Frictional velocity-weakening in landslides on Earth and on other planetary bodies. *Nature Communications*, *5*(1), 1–9.

Major, J., & Lara, L. (2013). Overview of Chaitén Volcano, Chile, and its 2008-2009 eruption. *Andean Geology*, *40*(2), 196–215.

Major, J., Pierson, T., Hobliltt, R., & Moreno, H. (2013). Pyroclastic density currents associated with the 2008-2009 eruption of Chaitén Volcano (Chile): Forest disturbances, deposits, and dynamics. *Andean Geology*, *40*(2), 324–358.

Malin, M., & Sheridan, M. (1982). Computer-assisted mapping of pyroclastic surges. *Science*, *217*(4560), 637–640. https://doi.org/10.1126/science.217.4560.637

Murcia, H., Sheridan, M., Macías, J., & Cortés, G. (2010). TITAN2D simulations of pyroclastic flows at Cerro Machín Volcano, Colombia: Hazard implications. *Journal of South American Earth Sciences*, *29*(2), 161–170. https://doi.org/10.1016/j.jsames.2009.09.005

Nakada, S. (2000). Hazards from pyroclastic flows and surges. *Encyclopedia of Volcanoes*, edited. New York: Elsevier.

Neri, A., Bevilacqua, A., Esposti Ongaro, T., Isaia, R., Aspinall, W., Bisson, M., et al. (2015). Quantifying volcanic hazard at Campi Flegrei caldera (Italy) with uncertainty assessment: 2. Pyroclastic density current invasion maps. *Journal of Geophysical Research: Solid Earth*, *120*, 2330–2349. https://doi.org/10.1002/2014JB011776

Neri, A., Esposti Ongaro, T., Macedonio, G., & Gidaspow, D. (2003). Multiparticle simulation of collapsing volcanic columns and pyroclastic flow. *Journal of Geophysical Research: Solid Earth*, *108*, 2202. https://doi.org/10.1029/2001JB000508

Neri, A., Esposti Ongaro, T., Voight, B., & Widiwijayanti, C. (2015). Pyroclastic density current hazards and risk. In *Volcanic hazards, risks and disasters* (pp. 109–140). Amsterdam: Elsevier.

Ogburn, S. E., & Calder, E. S. (2017). The relative effectiveness of empirical and physical models for simulating the dense undercurrent of pyroclastic flows under different emplacement conditions. *Frontiers in Earth Science*, *5*, 83. https://doi.org/10.3389/feart.2017.00083

Pudasaini, S., & Domnik, B. (2009). Energy considerations in accelerating rapid shear granular flows. *Nonlinear Processes in Geophysics*, *16*(3), 399–407. https://doi.org/10.5194/npg-16-399-2009

Pudasaini, S., & Hutter, K. (2007). *Avalanche dynamics: Dynamics of rapid flows of dense granular avalanches*. Berlin Heidelberg: Springer Science & Business Media.

Rabus, B., Eineder, M., Roth, A., & Bamler, R. (2003). The shuttle radar topography mission—A new class of digital elevation models acquired by spaceborne radar. *ISPRS Journal of Photogrammetry and Remote Sensing*, *57*(4), 241–262. https://doi.org/10.1016/S0924-2716(02)00124-7

Roche, O., Buesch, D. C., & Valentine, G. A. (2016). Slow-moving and far-travelled dense pyroclastic flows during the Peach Spring super-eruption. *Nature Communications*, *7*(1), 1–8.

Roche, O., Phillips, J., & Kelfoun, K. (2013). Pyroclastic density currents. In *Modeling volcanic processes: The physics and mathematics of volcanism* (pp. 203–229). Cambridge: Cambridge University Press.

Sandri, L., Thouret, J., Constantinescu, R., Biass, S., & Tonini, R. (2014). Long-term multi-hazard assessment for El Misti volcano (Peru). *Bulletin of Volcanology*, *76*(2), 771. https://doi.org/10.1007/s00445-013-0771-9

Sandri, L., Tierz, P., Costa, A., & Marzocchi, W. (2018). Probabilistic hazard from pyroclastic density currents in the Neapolitan area (Southern Italy). *Journal of Geophysical Research: Solid Earth*, *123*, 3474–3500. https://doi.org/10.1002/2017JB014890

Saucedo, R., Macías, J., Sheridan, M., Bursik, M. I., & Komorowski, J. (2005). Modeling of pyroclastic flows of Colima Volcano, Mexico: Implications for hazard assessment. *Journal of Volcanology and Geothermal Research*, *139*(1–2), 103–115. https://doi.org/10.1016/j.jvolgeores.2004.06.019

Shea, T., Gurioli, L., Houghton, B., Cioni, R., & Cashman, K. (2011). Column collapse and generation of pyroclastic density currents during the AD 79 eruption of Vesuvius: The role of pyroclast density. *Geology*, *39*(7), 695–698. https://doi.org/10.1130/G32092.1

Sheridan, M. (1979). Emplacement of pyroclastic flows: A review. *Geological Society of America Special Papers*, *180*, 125–136. https://doi.org/10.1130/SPE180-p125

Sheridan, M., Hubbard, B., Carrasco-Núñez, G., & Siebe, C. (2004). Pyroclastic flow hazard at Volcán Citlaltépetl. *Natural Hazards*, *33*(2), 209–221. https://doi.org/10.1023/B:NHAZ.0000037028.89829.d1

Sheridan, M., & Malin, M. (1983). Application of computer-assisted mapping to volcanic hazard evaluation of surge eruptions: Vulcano, Lipari, and Vesuvius. *Journal of Volcanology and Geothermal Research*, *17*(1–4), 187–202. https://doi.org/10.1016/0377-0273(83)90067-7

Sulpizio, R., Dellino, P., Doronzo, D., & Sarocchi, D. (2014). Pyroclastic density currents: State of the art and perspectives. *Journal of Volcanology and Geothermal Research*, *283*, 36–65.

Tierz, P., Sandri, L., Costa, A., Sulpizio, R., Zaccarelli, L., Di Vito, M., & Marzocchi, W. (2016). Uncertainty assessment of pyroclastic density currents at Mount Vesuvius (Italy) simulated through the energy cone model. *Natural Hazard Uncertainty Assessment: Modeling and Decision Support*, *223*, 125–145.

Tierz, P., Sandri, L., Costa, A., Zaccarelli, L., Di Vito, M., Sulpizio, R., & Marzocchi, W. (2016). Suitability of energy cone for probabilistic volcanic hazard assessment: Validation tests at Somma-Vesuvius and Campi Flegrei (Italy). *Bulletin of Volcanology*, *78*(11), 79. https://doi.org/10.1007/s00445-016-1073-9

Todesco, M., Neri, A., Esposti Ongaro, T., Papale, P., & Rosi, M. (2006). Pyroclastic flow dynamics and hazard in a caldera setting: Application to Phlegrean Fields (Italy). *Geochemistry, Geophysics, Geosystems*, *7*, Q11003. https://doi.org/10.1029/2006GC001314

Valentine, G., Perry, F., & WoldeGabriel, G. (2000). Field characteristics of deposits from spatter-rich pyroclastic density currents at Summer Coon volcano, Colorado. *Journal of Volcanology and Geothermal Research*, *104*(1–4), 187–199. https://doi.org/10.1016/S0377-0273(00)00206-7

Wadge, G., & Isaacs, M. (1988). Mapping the volcanic hazards from Soufriere Hills Volcano, Montserrat, West Indies using an image processor. *Journal of the Geological Society*, *145*(4), 541–551. https://doi.org/10.1144/gsjgs.145.4.0541

Walker, G. (1983). Ignimbrite types and ignimbrite problems. *Journal of Volcanology and Geothermal Research*, *17*(1–4), 65–88. https://doi.org/10.1016/0377-0273(83)90062-8

Woods, A., Bursik, M., & Kurbatov, A. (1998). The interaction of ash flows with ridges. *Bulletin of Volcanology*, *60*(1), 38–51. https://doi.org/10.1007/s004450050215